ROBOTIC AUTOMATION DISCOVERY OF BIODEGRADABLE ELECTRONICS VIA MULTIMODAL ACTIVE LEARNING AND AI-GUIDED DESIGN

Anonymous authors
Paper under double-blind review

ABSTRACT

Designing biodegradable electronic substrates that possess both mechanical robustness and tunable dielectric properties is a complex challenge, characterized by high-dimensional formulation spaces and nonlinear coupling between material properties. To accelerate discovery, we introduce a multimodal dynamic active learning (AL) framework integrated with multiple robotic automation platforms to navigate a vast design space with a 19-component library comprising biopolymers, layered clays, and metal oxides. Unlike static acquisition strategies, this AL framework employs a stage-wise approach that dynamically adapts sampling objectives, shifting from diversity-driven exploration to uncertainty-aware exploitation, to navigate the design space efficiently. This predictive modeling engine is tightly coupled with a fully automated experimental pipeline, featuring robotic liquid handling, automated tensile testing, and dielectric characterization, enabling closed-loop experimentation. Over eight AL rounds, we developed a prediction model leveraging an ensemble of hierarchical multimodal artificial neural networks for simultaneous feasibility screening and property prediction. Benchmarking demonstrates that this dynamic approach yields superior learning efficiency and target discovery compared to baselines under limited experimental budgets. We also successfully identified samples with mechanical robustness and an application-relevant range of dielectric properties demonstrating the practical utility of the closed-loop robotics–ML workflow under realistic experimental constraints.

1 INTRODUCTION

Electronics are deeply embedded across modern society, yet electronic waste has become one of the fastest-growing waste streams, contributing to landfills, ocean pollution, and persistent microplastic contamination (Law, 2017; Koelmans et al., 2022). Biopolymer-based biodegradable electronic substrates offer a promising route toward environmentally friendly devices for applications (Karavasili et al., 2026; Kamran et al., 2025) such as smart packaging, disposable sensors, wearable monitoring, and soft robotics. For practical use, such substrates need to possess mechanical robustness, ensuring handling and durability, and tunable dielectric behavior (Lopes et al., 2025; Feng et al., 2025) where high dielectric constants benefit capacitive components (e.g., energy-storage layers) and low dielectric constants are preferred for inductive elements (e.g., antennas and interconnects).

To meet these requirements, we consider a 19-component formulation library spanning layered clays, biopolymers, green additives, and metal oxides. While this formulation strategy enables broad property tunability, it creates a high-dimensional and strongly nonlinear design space in which mechanical and dielectric properties are tightly coupled. Conventional trial-and-error or one-factor-at-a-time experimentation becomes inefficient and provides limited insight into higher-order interactions. These challenges motivate machine learning (ML)-driven experimental design (Yang et al., 2026; Shrestha et al., 2024). Although Bayesian optimization (BO) (Chen et al., 2025; I. Allec & Ziatdinov, 2025) is effective in low-dimensional settings, its performance degrades in high-dimensional formulation spaces and batch-executed automated experiments.

To address these challenges, we introduce an automation-integrated, multi-stage dynamic active learning (AL) framework for the predictive design of biodegradable electronic substrates (Figure 1). The workflow first defines a feasible formulation space to systematically exclude low-quality and failure-prone samples. Experimental campaigns are then sequentially guided by a stage-wise AL strategy that adaptively balances exploration and exploitation as learning progresses. At each stage, candidate formulations are evaluated using an ensemble of multimodal hierarchical artificial neural networks (ANNs), which provide both predictive responses and associated uncertainty estimates. These uncertainty-aware predictions directly inform experiment selection, enabling efficient identification of informative and high-performing formulations under the small-dataset constraints typical of experimental materials research. Compared with baseline sampling strategies, including random sampling, diversity sampling, and BO, the proposed dynamic AL framework demonstrates superior learning efficiency and target discovery. Finally, by coupling predictive modeling with inverse design, we successfully identified nanocomposites with ultimate tensile strength (σ_u) and tensile toughness (U_T) up to ∼230 MPa and ∼24 MJ m^{-3}, respectively, while systematically mapping dielectric constants (κ) ranging from 2 to 200.

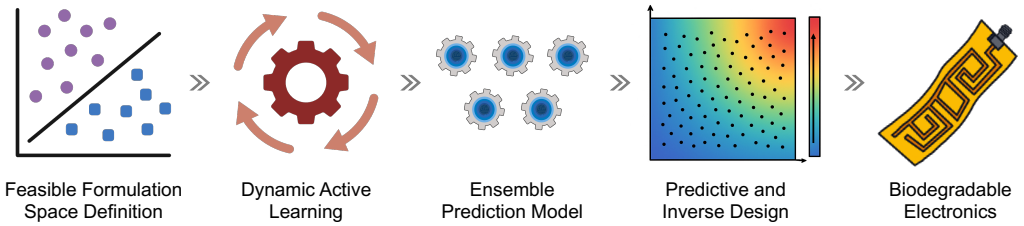

Figure 1: Workflow of accelerating Biodegradable Electronics Design(BioRender, a).

2 Hierarchical ANN Framework for Multimodal Learning

To support feasibility screening, dynamic AL, and inverse design within a unified modeling backbone, we employed a hierarchical ANN with a shared encoder and multiple branches for unique classification and regressions (Figure 2). A classifier head was activated for feasibility screening, while regression heads were activated during AL and inverse design to predict material properties.

The model architecture is defined as:

$$z = f_\theta(\mathbf{C}), \qquad \mathbf{C} \in \mathbb{R}^{19}, \tag{1}$$

$$y_t = \sigma(g_{\text{feas}}(z)), \qquad \text{feasibility classifier}, \tag{2}$$

$$y_p = g_p(z), \qquad p \in \{T_{\text{vis}}, \sigma_u, U_T, \kappa\}, \qquad \text{property regressor}, \tag{3}$$

where z is the shared encoder, $f_{\boldsymbol{\theta}}$ is parameterized by weights $\boldsymbol{\theta}$, g_{feas} denotes the feasibility head, $\sigma(\cdot)$ is the sigmoid function, and g_p is the task-specific regressor head for property p. Since all tasks share the same material system, feasibility-only data can be used to train the shared encoder, while property-labeled data further refine the encoder and task-specific heads, maximizing data efficiency under limited experimental budgets. The modular multi-branch design also allows new property heads to be added as data become available, enabling scalable model expansion without retraining or degrading previously learned representations. Overall, this hierarchical, phase-aware architecture supports efficient task transfer and uncertainty estimation, making it well suited for small-data, high-dimensional, and failure-prone experimental discovery.

3 Definition of Feasible Formulation Space

In biodegradable nanocomposite systems, experimental failures are costly due to time- and labor-intensive reformulation and refabrication, particularly when low-quality films are produced. This challenge is exacerbated by the high dimensionality of the 19-component formulation space (Appendix A), which renders systematic grid searches impractical (Appendix B). To improve experimental efficiency, we first defined a feasible formulation space that excluded failure-prone candidates prior to dynamic AL (Appendix C; Figure 4).

The feasible formulation space was constructed using a two-stage, Monte Carlo-based complementary sampling strategy (Hung, 2024). Diversity-driven sampling (Appendix C.1) was first employed to maximize coverage of the formulation space, after which an ANN ensemble was trained to guide uncertainty-based sampling (Appendix C.2) and refine the feasibility boundary. The resulting classifier achieved an accuracy of approximately 93% on an independent held-out test set (Appendix D). Additionally, SHapley Additive exPlanations (SHAP) analysis quantified the contribution of individual component loadings to feasibility predictions (Appendix E).

4 Multi-Stage Dynamic Active Learning

Starting from the feasible formulation space, we implemented a dynamic AL loop with a stage-wise acquisition function to guide exploration and exploitation of mechanical and dielectric properties (Figure 2, Appendix F). All formulations were fabricated and characterized using automation platforms, enabling consistent execution and rapid experimental feedback.

Property prediction was performed using an ensemble of hierarchical ANNs with property prediction heads. Data augmentation was employed to stabilize learning in the small-data regime and prevent overfitting (Appendix F.1). Predictive uncertainty, estimated from ensemble variance, was explicitly incorporated into data acquisition. Candidate formulations were selected using a dynamic acquisition function integrating formulation diversity, model uncertainty, and predicted performance:

$$A(\mathbf{C}) = \left(\tilde{D}(\mathbf{C})\right)^{n_s} \cdot \left(\tilde{\sigma}_p(\mathbf{C})\right)^{m_s} \cdot \left(\tilde{\mu}_p(\mathbf{C})\right)^{l_s}, \tag{4}$$

where $\tilde{D}(\mathbf{C})$ denotes the normalized minimum Euclidean distance between $\mathbf{C}$ and existing formulations, thereby promoting exploration of under-sampled regions. $\tilde{\sigma}_p(\mathbf{C})$ and $\tilde{\mu}_p(\mathbf{C})$ represents the normalized ensemble prediction standard deviation and mean for property. The exponents (n_s, m_s, l_s) were stage-specific hyperparameters that adapt the exploration–exploitation balance over the course of learning. Rather than relying on a fixed acquisition rule, sampling objectives were adaptively adjusted across three stages. Stage 1 emphasized diversity-driven exploration to broadly sample the feasible formulation space. Stage 2 balanced exploration and exploitation to refine model fidelity and identify mechanically promising regions. Stage 3 prioritized exploitation of mechanical performance while maintaining exploration along the dielectric dimension, enabling tunable dielectric design within mechanically robust formulation families (Appendix F.2).

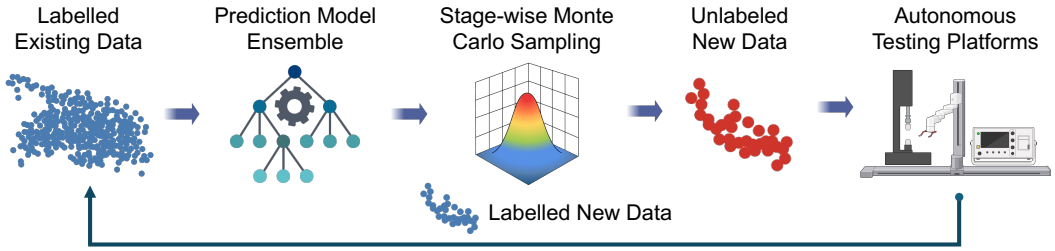

Figure 2: Workflow of dynamic AL strategy (BioRender, b).

Automated experimental characterization is a critical component of the proposed workflow, providing reliable, high-throughput feedback to support dynamic AL (Appendix G). The automation pipeline comprises three modules: (1) automated sample preparation using an OT-2 liquid-handling robot (Figure 9); (2) an automated tensile-testing platform integrating a collaborative robotic manipulator (UR5e) with a universal testing machine (Instron) (Figure 10); and (3) an automated dielectric characterization platform combining a custom-built robotic stage with an impedance analyzer (Figure 11). Together, the automation pipeline enabled consistent, low-latency acquisition of mechanical and dielectric data and support batch experimentation. Their tight integration with model retraining established a closed-loop experimental workflow that accelerated data acquisition and learning efficiency in high-dimensional materials design.

5 BENCHMARKING DYNAMIC AL AND INVERSE DESIGN OF BIODEGRADABLE ELECTRONIC SUBSTRATES

Over the eight rounds of dynamic AL, the framework progressively identified nanocomposites with σ_u up to ∼230 MPa and U_T up to ∼24 MJ m^{-3}, while systematically exploring dielectric constants spanning 2 to 200 regime (Appendix H.1). The final ensemble model achieved prediction accuracy (17%) comparable to experimental variability (∼15%) (Appendix H.2).

The proposed multi-stage dynamic AL strategy was benchmarked against three representative baselines, random sampling, diversity sampling, and BO, under identical experimental budgets of 300 formulations over 128 independent runs for σ_u and U_T (Appendix H.3). Random and diversity-based sampling, governed by stationary acquisition rules, exhibited early performance saturation, while BO achieved moderate improvements but showed diminished returns in the high-dimensional formulation space with limited budgets. In contrast, the dynamic AL strategy consistently achieved the highest predicted mechanical performance, reaching substantially higher σ_u and U_T within the same budget (Figure 3, with stage transitions indicated). The results are summarized in Table 2. These results demonstrate that stage-wise, non-stationary acquisition provides a clear advantage over static sampling strategies for efficient navigation of complex materials design spaces.

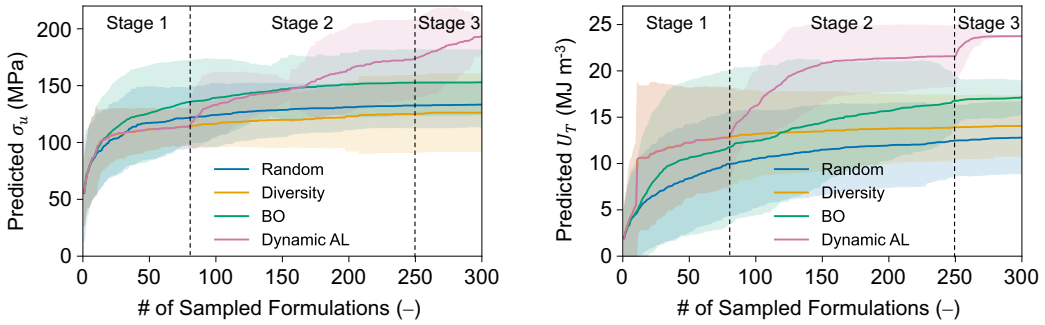

Figure 3: Benchmarking dynamic AL against baseline sampling strategies. Solid curves represent average values, and shaded regions represent the prediction variations across 128 runs.

Using predictive and inverse design, we identified biodegradable nanocomposite formulations that achieved the σ_u, U_T and κ tunability required for electronic substrates (Appendix I). Large-scale virtual screening of feasible compositions revealed distinct formulation families that satisfy combined strength, toughness, and dielectric constraints, enabling both low-κ substrates for inductive components and high-κ substrates for capacitive applications. These results demonstrate that mechanically durable, functionally diverse biodegradable electronics can be rationally designed across a wide property range, providing practical guidance for sustainable electronic materials development.

6 CONCLUSION AND FUTURE WORK

In this work, we present a robotic automation-integrated dynamic AL framework for the discovery of biodegradable electronics in a high-dimensional space. The proposed workflow efficiently balances exploration and exploitation for nanocomposites exhibiting strong mechanical performance and tunable dielectric properties. Benchmarking against baseline strategies further demonstrates the advantage of stage-aware dynamic acquisition strategies for complex materials design problems.

Future work will extend this framework in three directions. First, incorporating polymer structural representations (e.g., SMILES) will enable chemistry-aware learning beyond formulation-level composition. Second, large language model–assisted literature mining will expand training datasets by extracting reported compositions, processing conditions, and properties. Third, physics-based simulations will be integrated as complementary feedback, with molecular dynamics predicting mechanical responses and electromagnetic modeling estimating device-level capacitive and inductive performance. Together, these advances will enable multi-fidelity, data-efficient discovery and accelerate translation from material formulations to functional biodegradable electronics.

REFERENCES

BioRender. BioRender, a. URL https://app.biorender.com/citation/697fd09bb576f7b3aeae2c00.

BioRender. BioRender, b. URL https://app.biorender.com/citation/697fd2a353f6bda4f32c0bab.

BioRender. BioRender, c. URL https://app.biorender.com/citation/697fd4d10362eb7c308a7a13.

BioRender. BioRender, d. URL https://app.biorender.com/citation/697fd5a5f4fd11b8061d0006.

Junhe Chen, A. N. M. Nafiz Abeer, Alif Bin Abdul Qayyum, Zhihao Feng, Hyun-Myung Woo, Byung-Jun Yoon, and Seung Soon Jang. Accelerated Discovery of High-Performance Polyamines for Solid-State Direct CO$_2$ Capture via Efficient Simulations and Bayesian Optimization. October 2025. URL https://openreview.net/forum?id=aECXy5Jgm4.

Tianle Chen, Zhenqian Pang, Shuaiming He, Yang Li, Snehi Shrestha, Joshua M. Little, Haochen Yang, Tsai-Chun Chung, Jiayue Sun, Hayden Christopher Whitley, I.-Chi Lee, Taylor J. Woehl, Teng Li, Liangbing Hu, and Po-Yen Chen. Machine intelligence-accelerated discovery of all-natural plastic substitutes. *Nature Nanotechnology*, 19(6):782–791, June 2024. ISSN 1748-3395. doi: 10.1038/s41565-024-01635-z. URL https://www.nature.com/articles/s41565-024-01635-z.

Miaoyun Feng, Guixuan Lu, Zihao Wang, and Ying Jiang. Wireless technologies in stretchable bioelectronics. *J. Mater. Chem. C*, 13(40):20334–20366, 2025. doi: 10.1039/D5TC02191J. URL http://dx.doi.org/10.1039/D5TC02191J.

Ying-Chao Hung. A review of Monte Carlo and quasi-Monte Carlo sampling techniques. *WIREs Computational Statistics*, 16(1):e1637, 2024. ISSN 1939-0068. doi: 10.1002/wics.1637. URL https://onlinelibrary.wiley.com/doi/abs/10.1002/wics.1637. _eprint: https://wires.onlinelibrary.wiley.com/doi/pdf/10.1002/wics.1637.

Sarah I. Allec and Maxim Ziatdinov. Active and transfer learning with partially Bayesian neural networks for materials and chemicals. May 2025. doi: 10.1039/D5DD00027K. URL https://pubs.rsc.org/en/content/articlehtml/2025/dd/d5dd00027k.

Farimah Kamran, Hana Afshar, and Farangis Shahi. Recent Advances and Applications of Sustainable and Recyclable Polymers. *Polymer Engineering & Science*, 65(8):3845–3879, 2025. ISSN 1548-2634. doi: 10.1002/pen.27257. URL https://onlinelibrary.wiley.com/doi/abs/10.1002/pen.27257. _eprint: https://4spepublications.onlinelibrary.wiley.com/doi/pdf/10.1002/pen.27257.

Dimitra Karavasili, Kyriaki Lazaridou, Maria Angeliki Ntrivala, Andreas Chrysovalantis Pitsavas, Zafeiria Baziakou, Maria Papadimitriou, Nikolaos D. Bikiaris, Evangelia Balla, and oi Terzopoulou. Biobased Polymers in Printed Electronics: From Renewable Resources to Functional Devices. *Polymers*, 18(2):301, January 2026. ISSN 2073-4360. doi: 10.3390/polym18020301. URL https://www.mdpi.com/2073-4360/18/2/301.

Albert A. Koelmans, Paula E. Redondo-Hasselerharm, Nur Hazimah Mohamed Nor, Vera N. de Ruijter, Svenja M. Mintenig, and Merel Kooi. Risk assessment of microplastic particles. *Nature Reviews Materials*, 7(2):138–152, February 2022. ISSN 2058-8437. doi: 10.1038/s41578-021-00411-y. URL https://www.nature.com/articles/s41578-021-00411-y.

Kara Lavender Law. Plastics in the Marine Environment. *Annual Review of Marine Science*, 9(Volume 9, 2017):205–229, January 2017. ISSN 1941-1405, 1941-0611. doi: 10.1146/annurev-marine-010816-060409. URL https://www.annualreviews.org/content/journals/10.1146/annurev-marine-010816-060409.

Thomaz Jacintho Lopes, Ary Machado de Azevedo, Sergio Neves Monteiro, and Fernando Manuel Araujo-Moreira. Electrical Properties of Composite Materials: A Comprehensive Review. *Journal of Composites Science*, 9(8):438, August 2025. ISSN 2504-477X. doi: 10.3390/jcs9080438. URL https://www.mdpi.com/2504-477X/9/8/438.

Scott M Lundberg and Su-In Lee. A Unified Approach to Interpreting Model Predictions. In *Advances in Neural Information Processing Systems*, volume 30. Curran Associates, Inc., 2017. URL https://proceedings.neurips.cc/paper/2017/hash/8a20a8621978632d76c43dfd28b67767-Abstract.html.

Snehi Shrestha, Kieran James Barvenik, Tianle Chen, Haochen Yang, Yang Li, Meera Muthachi Kesavan, Joshua M. Little, Hayden C. Whitley, Zi Teng, Yaguang Luo, Eleonora Tubaldi, and Po-Yen Chen. Machine intelligence accelerated design of conductive MXene aerogels with programmable properties. *Nature Communications*, 15(1):4685, June 2024. ISSN 2041-1723. doi: 10.1038/s41467-024-49011-8. URL https://www.nature.com/articles/s41467-024-49011-8.

Haochen Yang, Qiongyu Chen, Tianle Chen, Yang Li, Elizabeth A. Norris, Joshua M. Little, Jiayue Sun, Snehi Shrestha, Edison Chen, Shenqiang Ren, Teng Li, and Po-Yen Chen. Predictive design of stretchable electrodes with strain-insensitive performance via robotics- and machine learning-integrated workflow. *Nature Communications*, January 2026. ISSN 2041-1723. doi: 10.1038/s41467-026-68484-3. URL https://www.nature.com/articles/s41467-026-68484-3.

APPENDICES

A Material Selection 7

B Estimated number of experiments required to build an extensive dataset 7

C Details on feasible formulation space definition 7

C.1 Diversity sampling 8

C.2 Uncertainty sampling 9

D Feasible formulation space classification results 9

E SHapley Additive exPlanations (SHAP) 10

F Implementation and Evaluation of Dynamic Active Learning Loops 12

F.1 Uncertainty-Informed Data Augmentation 12

F.2 Multi-Stage Monte Carlo Sampling with Dynamic Acquisition 13

G Autonomous Experimental Preparation, Characterization, and Feedback Integration. 13

G.1 Automation Sample Preparation 13

G.2 Automation Tensile Test 14

G.3 Automation Dielectric Test 14

G.4 Closed-loop model updating and feedback integration 15

H Performance and outcomes of dynamic active learning loops 16

H.1 Evolution of data distributions during dynamic active learning 16

H.2 Evaluation of Final model performance 18

H.3 Benchmarking Against Baseline and Model-Driven Sampling Strategies 18

I Predictive and Inverse Design of Biodegradable Electronic Substrates. 20

A MATERIAL SELECTION

Materials were selected through a combined literature frequency analysis, practical screening, and inclusion of emerging candidates with demonstrated potential for biodegradable electronic applications. This process yielded a robust and application-relevant library of 19 components, all of which are natural, bioderived, and/or Generally Recognized as Safe (GRAS), ensuring sustainability and experimental compatibility. The selected components were grouped into four functional categories according to their primary roles in the nanocomposite system: layered clays and biopolymers, which serve as the structural matrix and reinforcement; green additives, which modulate chain mobility and mechanical response; and metal oxide fillers, including both particulate and fibrous forms, which enable tuning of dielectric and mechanical properties. The complete list of materials and their classifications is provided in Table 1.

Table 1: 19-component material library serving as building blocks

Functional Category	**Materials**
Layered Clays	Laponite (LAP), montmorillonite (MMT)
Biopolymers	Cellulose nanocrystal (CNC), gelatin (GEL), chitosan (CHS), sodium alginate (ALG), carrageenan (CAR), sodium carboxymethyl cellulose (CMC), and silk (SLK)
Green Additives	Glycerol (GLY), xylitol (XYL), phytic acid (PHA), and lactic acid (LAC)
Metal Oxides	Magnesium oxide (MGO), zinc oxide (ZNO), titanium oxide (TIO), zirconium oxide (ZRO), silica fibers (SIF), and zirconium dioxide fibers (ZRF)

B ESTIMATED NUMBER OF EXPERIMENTS REQUIRED TO BUILD AN EXTENSIVE DATASET

Biobased nanocomposites were fabricated based on the rule of selecting any 4 components from 19 and mixing them at varying ratios. The total number of possible formulations (denoted as N) was estimated using Equation (5),

$$N = \binom{x}{4} \times \binom{k+3}{3}, \tag{5}$$

where x represents the total number of biobased components in the library (i.e., $x = 19$) and k corresponds to the number of steps from 0.0 to 100.0 wt.% (with a step size of 2.0 wt.%, $k = 50$). Through this equation, the total number of possible formulations was calculated to be 9.08×10^7.

The size of the candidate formulation space increases exponentially with the number of components. Increasing the number of selected components from two to seven expands the number of possible formulations from $\sim 10^6$ to $\sim 10^9$. Our materials library spans four functional categories: layered clays, biopolymers, green additives, and metal oxides. We constrained each formulation to four components because this choice captures cross-category interactions and preserves sufficient compositional complexity, while keeping the search space tractable for experimental sampling and for training predictive models with a realistic dataset size and computational cost. In contrast, allowing substantially higher-order mixtures would inflate the design space to an impractical scale and introduce redundant degrees of freedom (DOFs) that are difficult to learn reliably from limited experimental data.

C DETAILS ON FEASIBLE FORMULATION SPACE DEFINITION

Biobased nanocomposite fabrication is inherently time- and labor-intensive, and failed trials are particularly costly when model-suggested formulations yield films that are non-uniform or cannot be

detached. To reduce this experimental bottleneck, an ANN-based feasibility classifier was introduced as an explicit screening stage within both the AL loops and the inverse design process. This classifier filters candidate formulations prior to fabrication, enabling the learning system to focus on compositions with a high probability of producing feasible films (i.e., uniform and detachable). As a result, experimental failures are minimized, and experimental resources are concentrated on high-quality candidates.

Each sampling round followed a standardized workflow consisting of: (1) OT-2 robot-assisted mixture preparation, (2) air drying, (3) detachability and uniformity grading, (4) training the ANN-based feasibility classifier, and (5) selecting formulations for the next sampling round. Two complementary stages Monte Carlo-based sampling strategies were employed (Figure 4): diversity sampling to maximize coverage of the formulation space and uncertainty sampling to refine the feasibility boundary. Autonomous sampling preparation was executed by programming pipetting robots (OT-2). Resulting films were rapidly assessed for detachability and uniformity, and only formulations meeting both criteria were labeled feasible.

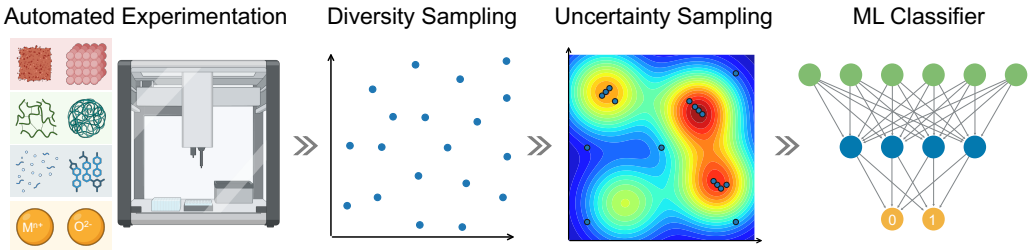

Figure 4: Workflow of building feasible formulation space classifier (BioRender, c).

C.1 Diversity Sampling

To construct a broad and representative training set for the ANN feasibility classifier, we employed a diversity-driven sampling strategy that maximizes coverage of the formulation space. Specifically, we maintained a candidate pool of N formulations and sought to maximize the minimum pairwise Euclidean distance among formulations in the pool. A Monte Carlo-based replacement procedure was used. First, an initial pool of N distinct formulations was randomly generated among the feasible parameter space. Each formulation was represented by a composition vector C_i defined by Equation (6):

$$C_i \in \Delta^M, \quad \Delta^M = \left\{ C \in \mathbb{R}^M_{\geq 0} : \sum_{j=1}^{M} C_{ij} = 1 \right\}, \tag{6}$$

where M is the number of components in the materials library ($M = 19$), and C_{ik} denotes the loading of component k in formulation C_i. For each formulation, we computed a distance score D_i as the minimum Euclidean distance to all other formulations currently in the pool by Equation (7):

$$D_i = \min_{i,j \in N, i \neq j} \|C_i - C_j\|_2 = \min_{i,j \in N, i \neq j} \sqrt{\sum_{k=1}^{M} (C_{ik} - C_{jk})^2}. \tag{7}$$

In each Monte Carlo iteration, a new formulation C_x was generated via random sampling, and its distance score D_x to current pool was evaluated as Equation (8):

$$D_x = \min_{i \in N, x \notin N} \|C_x - C_i\|_2 = \min_{i \in N, x \notin N} \sqrt{\sum_{k=1}^{M} (C_{xk} - C_{ik})^2}. \tag{8}$$

If D_x exceeded the minimum uncertainty score in the current pool, C_x replaced the lowest-scoring formulation; otherwise, C_x was discarded and the algorithm proceeded to the next iteration. This replacement scheme promotes a uniformly distributed and well-separated formulation set, thereby maximizing diversity in experimental sampling.

C.2 UNCERTAINTY SAMPLING

To further refine the feasibility classifier, we employed an uncertainty sampling strategy that prioritizes formulations exhibiting strong disagreement within a committee of multimodal hierarchical ANNs, while simultaneously preserving diversity in the sampled design space. During this stage, only the feasibility head of the multimodal ANN framework was activated to model the feasibility function and to estimate predictive uncertainty (Figure 5 left). A Monte Carlo-based replacement procedure was implemented. First, an initial pool containing N distinct formulations was randomly generated. Each formulation C_i was assigned an uncertainty score U_i, defined as the product of its minimum Euclidean distance to the remaining pool (diversity term, D_i) and the committee prediction variance (uncertainty term, $\text{Var}(C_i)$) shown in Equation (9):

$$U_i = D_i \cdot \text{Var}(C_i) = D_i \cdot \frac{1}{P} \sum_{l=1}^{P} \text{Var}_l(C_i). \tag{9}$$

The uncertainty term $\text{Var}(C_i)$ is the prediction variance estimated from an ANN committee with P models ($P = 5$), reflecting model disagreement for formulation C_i. In each Monte Carlo iteration, a new formulation C_x was randomly generated within the feasible design space, and its uncertainty score U_x was computed using Equation (10):

$$U_x = D_x \cdot \text{Var}(C_x) = D_x \cdot \frac{1}{P} \sum_{l=1}^{P} \text{Var}_l(C_x). \tag{10}$$

If U_x exceeded the minimum uncertainty score in the current pool, C_x replaced the lowest-scoring formulation; otherwise, C_x was discarded and the algorithm proceeded to the next iteration. This procedure continuously improves the candidate pool toward formulations that are both highly uncertain (informative for model refinement) and well separated (diverse), thereby enhancing classifier robustness and sampling efficiency.

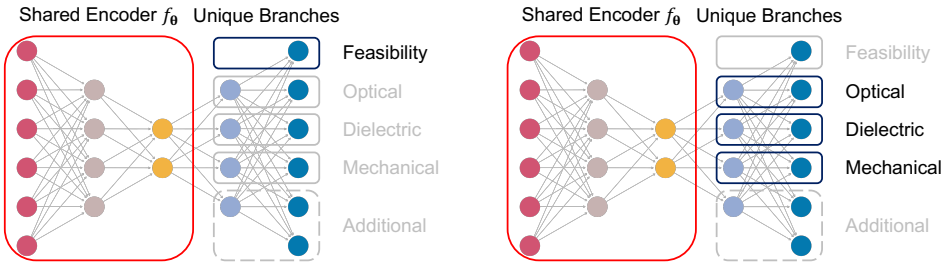

Figure 5: Framework of multimodal hierarchical ANNs. (Left) Classifier during feasible formulation space definition step. (Right) Regressor for property prediction during dynamic AL step (BioRender, d).

D FEASIBLE FORMULATION SPACE CLASSIFICATION RESULTS

2200 and 600 formulations were fabricated and labeled during diversity and uncertainty sampling stages, respectively. The final classifier achieved a classification accuracy of ∼93% on an independent held-out test set (500 formulations). The loading distributions of the 19 components across the 3300 nanocomposites (training + test formulations) was summarized in Figure 6, showing that each component was incorporated into ∼700 formulations with loadings spanning 0–80%, consistent with broad coverage of the formulation space.

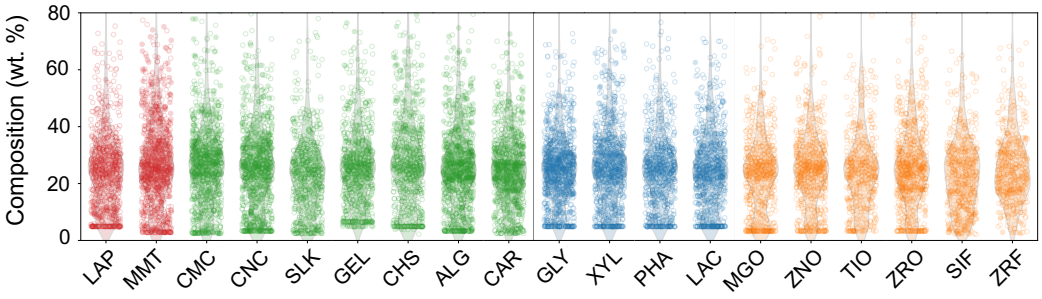

Figure 6: Loading distribution profile of 19 components across feasible formulation space definition phase. The dot color represents the predominant component category in each nanocomposite formulation: red is layered clay-rich, green is biopolymer-rich, and blue is green additive-rich, and orange is metal oxide-rich. The solid dots represent "feasible" nanocomposites, while the empty dots represent "infeasible" ones.

As shown in Figure 7, a dimensionality-reduction map was generated using the trained ANN feasibility classifier by extracting activations from the penultimate hidden layer as latent representations of each formulation. These high-dimensional embeddings were projected into a two-dimensional space to visualize the formulation landscape and feasibility structure. The resulting map reveals clear separation between feasible and infeasible nanocomposites, delineating the feasible design space and highlighting regions enriched with formulations predicted to yield uniform and detachable films.

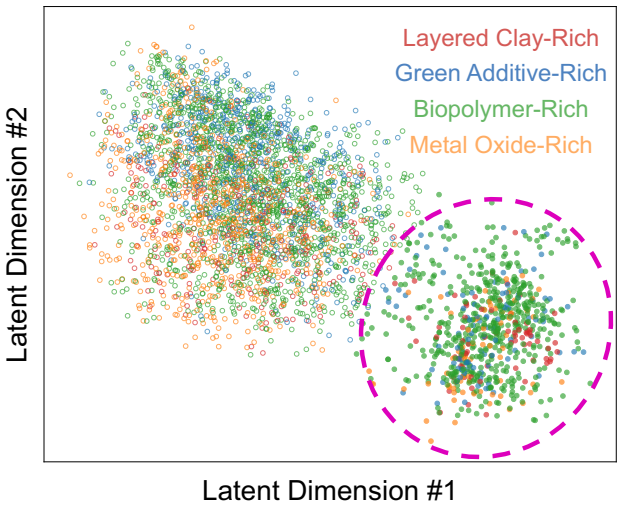

Figure 7: Visualization of feasibility classification dataset. The dot color represents the predominant component category in each nanocomposite formulation. The solid and empty dots represent "feasible" and "infeasible" nanocomposites, respectively.

E SHAPLEY ADDITIVE EXPLANATIONS (SHAP)

To interpret the trained prediction models (including ensemble predictors), we used SHAP (Lundberg & Lee, 2017), a game-theoretic framework that attributes a model's prediction to individual input features in a principled and model-agnostic manner. SHAP assigns each feature a contribution value (the Shapley value) such that the sum of feature contributions recovers the model output relative to a baseline expectation.

Consider a model $f(\mathbf{x})$ with M input features. SHAP expresses the prediction for a specific input x as an additive decomposition:

$$f(x) = E[f(X)] + \sum_{k=1}^{M} \phi_k, \tag{11}$$

where $E[f(X)]$ is the expected model output over the dataset (baseline), and ϕ_k is the SHAP value quantifying the contribution of feature k to the deviation of $f(x)$ from the baseline. Formally, ϕ_k is defined as the average marginal contribution of feature k over all possible subsets (coalitions) of features:

$$\phi_k = \sum_{S \subseteq F \setminus \{k\}} \frac{|S|!(M - |S| - 1)!}{M!} [f(S \cup \{k\}) - f(S)], \tag{12}$$

where F is the full feature set, and $f(S)$ denotes the model evaluated using only features in subset S (with remaining features marginalized according to the background data distribution). This definition ensures desirable axioms such as efficiency (attributions sum to the prediction), symmetry, and null effects (irrelevant features receive zero attribution).

In this work, each input feature corresponds to the loading (mass fraction) of one component in the formulation (e.g., 19 components). For each formulation x, the model prediction of a given property (e.g., T_{vis}, σ_u, U_T, or κ) is treated as the "payout," and SHAP values $\{\phi_k\}$ quantify how each component loading drives the predicted property relative to the baseline $E[f(X)]$. This yields a local interpretation for each data point and each predicted property. To obtain global interpretations, SHAP values were aggregated over all data points. Features exhibiting larger magnitudes and wider distributions of SHAP values (e.g., higher $|\phi_k|$ across the dataset) are interpreted as having stronger overall influence on model predictions. From the SHAP analysis shown in Figure 8, the components with the largest positive contributions to feasibility include MMT (layered clay), CMC, CNC, ALG, and CAR (biopolymers), GLY (green additive), and the fibrous metal oxides SIF and ZRF. In contrast, LAP (layered clay), SLK (biopolymer), PHA (green additive), and MGO (metal oxide) exhibited the strongest negative contributions, indicating that increasing their loadings tends to decrease the probability of forming feasible films.

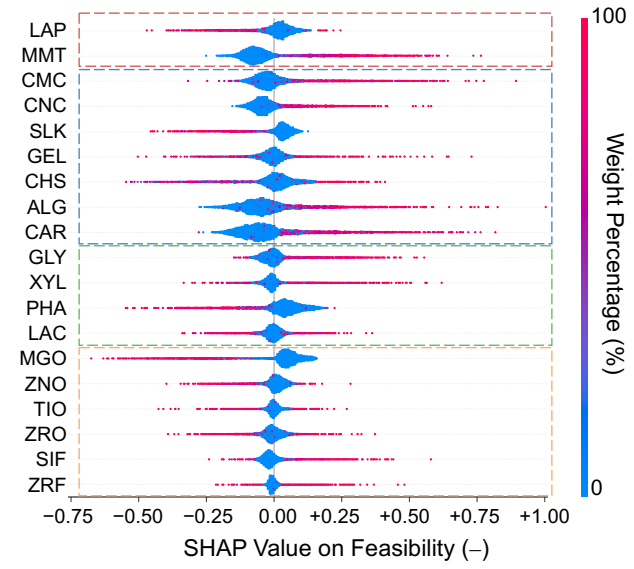

Figure 8: SHAP results of feasibility classification.

F Implementation and Evaluation of Dynamic Active Learning Loops

Fabrication and characterization of biobased nanocomposite films are inherently time- and labor-intensive, particularly for multi-property measurements involving optical, mechanical, and dielectric testing. These experimental costs are exacerbated by the combinatorial scale of the formulation space, rendering exhaustive exploration impractical. This appendix details the implementation of the proposed dynamic AL loops, which strategically select informative formulations to maximize learning efficiency under limited experimental budgets. By combining uncertainty-aware modeling, stage-wise acquisition, and automated experimentation, the workflow prioritizes high-impact experiments while minimizing redundant or low-information trials.

The AL workflow was initiated by randomly sampling a small batch of feasible formulations to establish baseline coverage of the formulation space. All samples were prepared using automated liquid-handling and casting procedures, followed by standardized drying conditions to produce free-standing films suitable for characterization. In each loop, hierarchical neural network ensembles are trained using augmented data, candidate formulations are selected via a stage-adaptive Monte Carlo acquisition strategy, and experimental feedback is generated through automated sample preparation and characterization platforms, thereby closing the learning loop.

F.1 Uncertainty-Informed Data Augmentation

To mitigate data scarcity during early learning stages and improve generalization under limited experimental budgets, we applied an in-silico data augmentation strategy termed uncertainty-informed perturbation (UIP) (Chen et al., 2024) prior to training the multi-property prediction models. UIP generates local, physically plausible virtual samples by injecting bounded noise into both formulation compositions and corresponding property labels, where perturbation magnitudes are informed by experimentally observed variability rather than unconstrained synthetic sampling. For each real formulation C_i (see Equation 6), UIP generates K virtual samples by perturbing only the active components and projecting the result back onto the simplex:

$$C_{i,k} = \Delta(C_i + \eta_{i,k}), \quad k \in \{1, \dots, K\}, \tag{13}$$

where $\Delta(\cdot)$ denotes Euclidean projection onto Δ^M. The perturbation vector $\eta_{i,k}$ is defined elementwise as

$$\eta_{i,k,j} = \begin{cases} \delta_{i,k,j}, & j \in S_i, \\ 0, & j \notin S_i, \end{cases} \tag{14}$$

with $S_i = \{j : C_{ij} > 0\}$ denoting the active component set. For active components, the perturbations are sampled from a truncated normal distribution:

$$\delta_{i,k,j} \sim \mathcal{TN}\left(0, (\sigma_c C_{ij})^2; -\beta_c C_{ij}, \beta_c C_{ij}\right), \quad j \in S_i, \tag{15}$$

where TN denotes a truncated normal distribution. Scaling the perturbation magnitude by the original component loading C_{ij} enforces relative perturbations, preserving sparsity structure and preventing unrealistic modification of trace components. For each predicted property $p \in \{\sigma_u, U_T, \kappa, \dots\}$, corresponding property labels are perturbed using bounded noise scaled by experimentally estimated uncertainty:

$$y_{i,k}(p) = y_i(p) + \epsilon_{i,k}(p), \tag{16}$$

$$\epsilon_{i,k}(p) \sim \mathcal{TN}\left(0, (\lambda_p u_i(p))^2; -\beta_p u_i(p), \beta_p u_i(p)\right), \tag{17}$$

where $u_i(p)$ denotes the experimentally estimated uncertainty for property p, obtained from replicate measurements and round-specific statistics. Truncation ensures that perturbed labels remain physically plausible and prevents extreme or nonphysical values. A virtual-to-real ratio of 100:1 was used in each AL round, providing sufficient diversity to stabilize model training and ensemble uncertainty estimation while maintaining training times below one day per iteration. To prevent overfitting to augmented data, UIP samples were used exclusively within training folds, with model selection performed on held-out validation sets. Early stopping and L2 regularization were additionally applied.

F.2 Multi-Stage Monte Carlo Sampling with Dynamic Acquisition

The ensemble framework provides both predicted mean responses and uncertainty estimates, quantified by the variance across ensemble members. These quantities were incorporated into a dynamic acquisition function that assigns each candidate formulation C an acquisition score (Equation 2): $A(C) = (D(C))^{n_s} \cdot (\sigma_p(C))^{m_s} \cdot (\mu_p(C))^{l_s}$, where $D(C)$ is the normalized minimum Euclidean distance to previously sampled formulations (promoting exploration), and $\sigma_p(C)$ and $\mu_p(C)$ are the normalized ensemble prediction standard deviation and mean for property p, respectively, provided by the regression heads of ANNs (Figure 5 right).

The exponents (n_s, m_s, l_s) are stage-dependent parameters controlling the exploration–exploitation balance. Sampling objectives evolved across three stages:

- Stage 1: emphasized diversity-driven exploration $(n_s, m_s, l_s) = (1, 0, 0)$ to broadly map the feasible formulation space.
- Stage 2: balanced exploration and exploitation $(n_s, m_s, l_s) = (1, 1, 1)$ for mechanical properties (σ_u or U_T), while treating κ as a tunable attribute using an exploration-focused mode $(n_s, m_s, l_s) = (1, 1, 0)$.
- Stage 3: further strengthened exploitation of mechanical performance $(n_s, m_s, l_s) = (1, 1, 4)$ while prioritizing uncertainty-driven exploration for κ, $(n_s, m_s, l_s) = (1, 4, 0)$, enabling efficient mapping of dielectric tunability within mechanically robust formulation families.

During Stages 2 and 3, dielectric exploration was constrained to formulations satisfying minimum mechanical thresholds ($\sigma_u > 30$ MPa or $U_T > 5$ MJ m^{-3}) to ensure practical relevance. Candidate formulations were selected via Monte Carlo sampling within the feasible formulation space, ranked by acquisition score, and filtered using a greedy diversity criterion to avoid near-duplicate compositions within each batch.

G Autonomous Experimental Preparation, Characterization, and Feedback Integration

Automated experimentation is a core component of the proposed workflow, enabling reliable, high-throughput feedback required for dynamic AL in a high-dimensional and failure-prone formulation space. Automation pipeline consists of sample preparation, mechanical characterization, and dielectric characterization, minimizing manual intervention while ensuring consistency and scalability.

G.1 Automation Sample Preparation

Formulation preparation was performed using an OT-2 liquid-handling robot, enabling high-throughput and reproducible mixture preparation. Each OT-2 batch processed up to 90 formulations for one batch without any human supervision. Due to the robot's maximum pipette capacity (1 mL), each formulation required multiple liquid-handling cycles, resulting in more than 800 pipetting actions per batch. Highly viscous components (e.g., CMC, CHS, and ALG) were handled using reduced aspiration and dispensing speeds, programmed pauses, and multi-step dispensing to ensure volumetric accuracy. The automated preparation of one batch required approximately 8 h of machine time.

To ensure reproducible execution and reliable data integration across the automated pipeline, we developed a unified sample identification, tracking, and OT-2 protocol generation system. A standardized sample ID schema was introduced and coupled with custom sticker labels to maintain consistent mapping between physical samples and digital records throughout formulation, drying, and characterization. This infrastructure enforces traceability, reduces human error, and supports reproducible data generation for machine-learning-driven experimentation. To lower the barrier to adoption and promote reproducibility, we further implemented a user-accessible OT-2 protocol generation tool that allows users without programming experience to generate validated OT-2 scripts.

As shown in Figure 9 (left), the OT-2 robot performs automated mixture preparation. Figure 9 (middle) illustrates representative labels used across the workflow: red and green labels identify source

solution tubes and target mixture tubes, respectively; brown labels mark drying substrates during film fabrication; and blue labels containing sample ID and composition are applied to finalized samples for downstream characterization. Each blue label includes a QR code, enabling automatic linkage of experimental measurements to the central database. As shown in Figure 9 (right), we developed a protocol generation system that integrates modular inputs for formulation specification, solution inventory, and sampling configuration. Once these inputs are provided, the system automatically generates validated OT-2 execution protocols together with corresponding sample labels, ensuring standardized, auditable, and scalable experimental execution aligned with ML-ready data pipelines. By abstracting low-level robot control and pipetting logic into a user-facing interface, this infrastructure enables researchers without programming expertise to run autonomous experiments while producing reproducible datasets that can be seamlessly incorporated into feedback-driven learning loops.

Figure 9: Automated sample preparation and OT-2 protocol management system. (Left) OT-2 liquid-handling robot. (Middle) Representative sample identification and tracking interface. (Right) User-facing OT-2 protocol generation and laboratory automation dashboard.

G.2 Automation Tensile Test

Mechanical properties were measured using a fully automated tensile-testing platform that tightly integrates a collaborative robotic manipulator (UR5e) with a universal testing machine (Instron). In this system, the robotic arm autonomously executed the entire sample-handling sequence, including pick-up, alignment, and insertion of freestanding nanocomposite films into the tensile grips, eliminating manual intervention and operator-dependent variability. Once loaded, uniaxial tensile tests were performed under standardized strain-rate and environmental conditions, ensuring consistency across large experimental batches. During testing, stress–strain responses were acquired in real time and automatically processed to extract key mechanical metrics, including ultimate tensile strength and tensile toughness. These properties were computed directly from the measured curves using predefined analysis routines and were programmatically returned to the central database and learning model without manual post-processing.

G.3 Automation Dielectric Test

Dielectric properties were characterized using a custom-built automated measurement stage integrated with an impedance analyzer, enabling high-throughput and reproducible dielectric constant measurements across large formulation batches. Nanocomposite films were mounted in modular sample racks, where each sample was sandwiched between two electrodes to ensure consistent electrical contact. Each rack accommodates six samples, and the robotic stage can load up to nine racks simultaneously. During operation, a motorized probe head connected to the impedance analyzer sequentially contacted each sample, performing automated dielectric measurements while traversing the array along programmed X–Y trajectories. This design enabled fully autonomous batch characterization, allowing up to 54 samples to be measured within approximately 2.5 hours under standardized conditions.

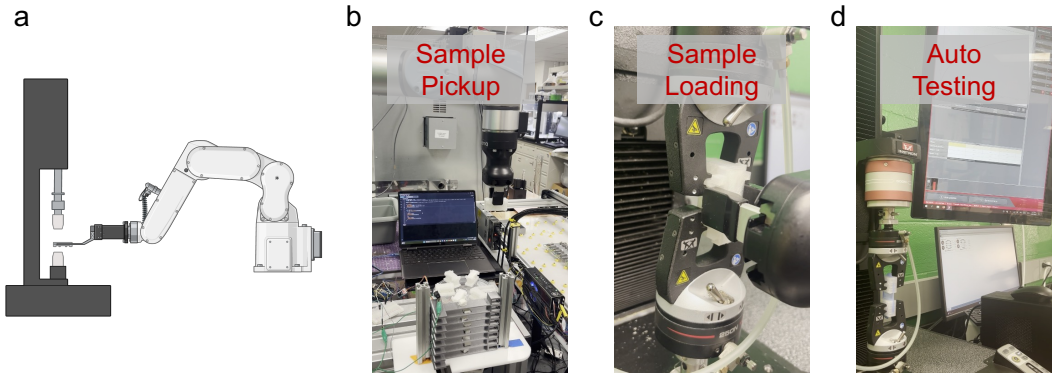

Figure 10: Automated tensile-testing platform for mechanical characterization. (a) Schematic illustration of the collaborative robotic tensile-testing system integrating a UR5e manipulator with an Instron universal testing machine. (b) Autonomous sample pick-up from the staging area by the robotic arm. (c) Robotic alignment and loading of the freestanding film into the tensile grips. (d) Automated uniaxial tensile testing and stress–strain data acquisition used to extract ultimate tensile strength and tensile toughness.

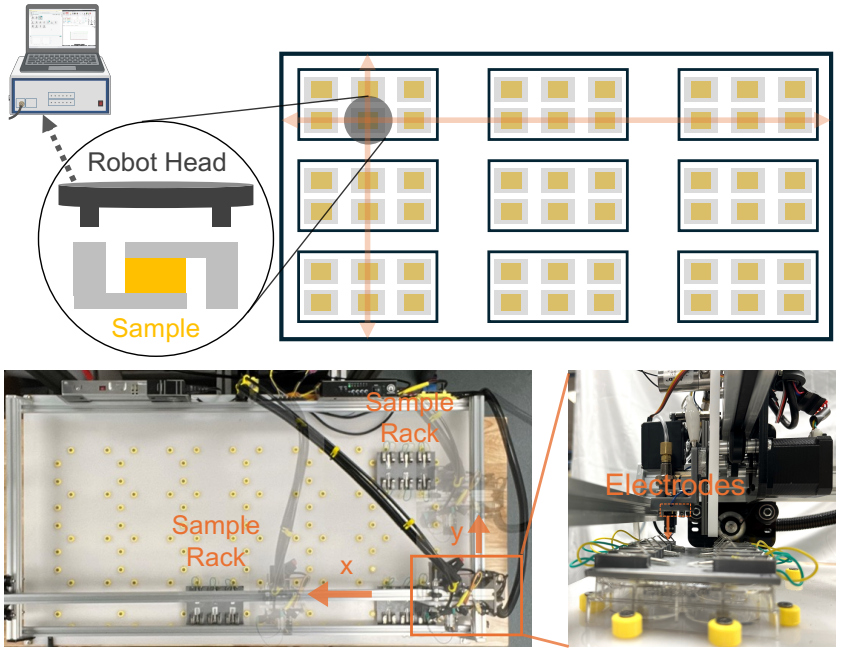

Figure 11: Automated dielectric characterization platform integrating a robotic X–Y stage with impedance spectroscopy for high-throughput, sequential measurement of dielectric properties across batched nanocomposite samples.

G.4 Closed-loop model updating and feedback integration

At the completion of each acquisition round, all experimentally measured properties were automatically appended to the central dataset and incorporated into the next model training cycle. The ensemble prediction models were retrained using the expanded dataset, together with uncertainty-informed data augmentation, enabling continuous refinement of both predictive accuracy and uncertainty estimation. This retraining step updated the acquisition function used in subsequent sampling rounds, ensuring that experimental feedback directly informs future decision-making. By tightly integrating

automated formulation, high-throughput characterization, and iterative model retraining, the workflow maintained a low-latency closed feedback loop between physical experimentation and learning. This closed-loop structure was critical for efficient feedback-based learning in high-dimensional, failure-prone materials design spaces, allowing sampling strategies to adapt dynamically as new information is acquired and enabling progressive convergence toward high-value formulation regions under constrained experimental budgets.

H PERFORMANCE AND OUTCOMES OF DYNAMIC ACTIVE LEARNING LOOPS

This section summarizes the outcomes of the multi-stage dynamic AL campaign, which converged in eight acquisition rounds comprising 286 experimentally characterized formulations. Over the course of learning, the framework progressively identified nanocomposites with ultimate tensile strength up to $\sim$230 MPa and tensile toughness up to $\sim$24 MJ m^{-3}, while systematically exploring dielectric constants spanning 2 to 200 regimes relevant for various electronic applications. The final ensemble prediction model achieved a mean relative error of $\sim$17%, comparable to experimental variability, and the sampling efficiency was benchmarked against random sampling, diversity sampling, and BO.

H.1 EVOLUTION OF DATA DISTRIBUTIONS DURING DYNAMIC ACTIVE LEARNING

Across eight AL loops, the framework progressively reshaped the sampled formulation distribution as acquisition objectives transitioned from global exploration to targeted exploitation. In total, 286 formulations were fabricated and characterized, spanning two loops of diversity-driven exploration (Stage 1), four loops of balanced exploration–exploitation (Stage 2), and two loops of objective-focused refinement (Stage 3). Figure 12 visualizes the evolution of component loading distributions across all loops. In these maps, circle diameters represent the recommended loading fractions of the 19 components, with larger diameters indicating higher suggested loadings. For σ_u optimization, the model converged toward formulations dominated by synergistic combinations of MMT, ALG, and CAR, with cumulative loadings exceeding 75 wt.% in later stages. In contrast, U_T optimization revealed two distinct formulation families: (i) CHS-rich systems plasticized with GLY and XYL, and (ii) CNC/CMC-based systems incorporating similar plasticizer levels. For κ exploration, sampling was constrained to mechanically viable formulations, leading to preferential selection of robust biopolymer and clay components while systematically varying metal oxide additives to expand the accessible dielectric response space.

Property distributions evolved in a stage-dependent manner (Figure 13). Initial exploration yielded moderate mechanical performance ($\sigma_u \approx 80$ MPa, $U_T \approx 4$ MJ m^{-3}), whereas later stages rapidly concentrated samples in high-strength and high-toughness regimes, ultimately achieving $\sigma_u \approx 230$ MPa and $U_T \approx 24$ MJ m^{-3}. In parallel, dielectric constants expanded from a narrow low-κ regime (¡25) to a broader, tunable range (25–75), with selected formulations exhibiting values up to $\sim$200, while remaining constrained to mechanically robust compositions.

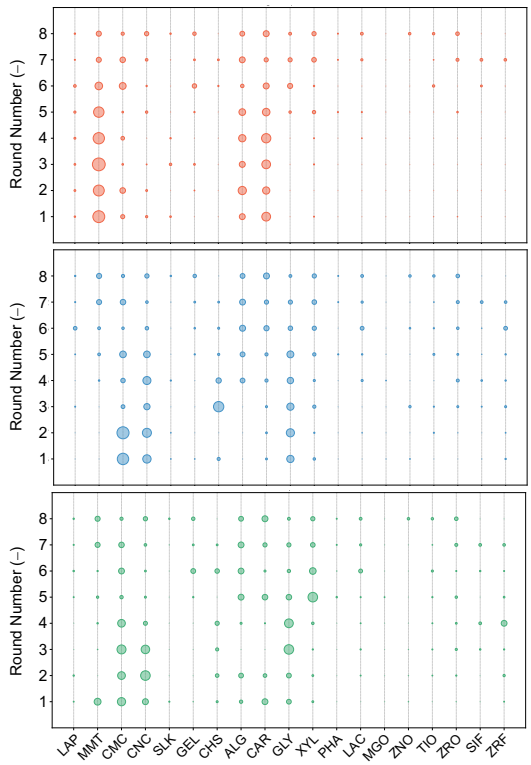

Figure 12: Mean weight percentages of 19 components recommended by the prediction model during eight AL loops, with optimization design of σ_u (red) and U_T (blue) and tunable design of κ (green).

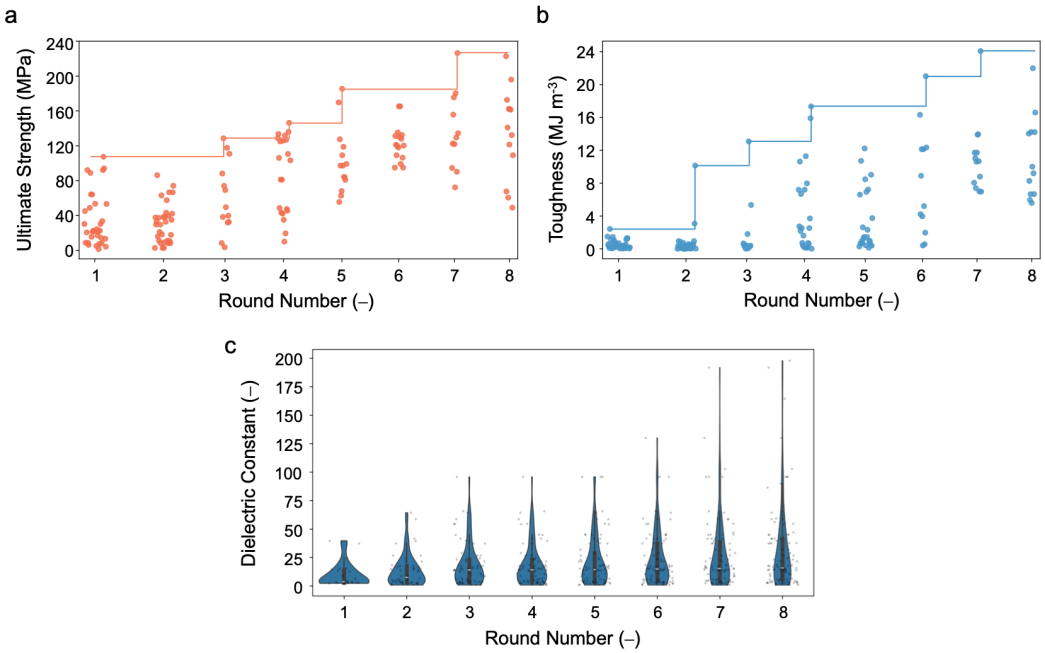

Figure 13: Property distributions during AL loops. Solid dots represent the characterized values, and solid lines represent the highest recorded values: (a) σ_u and (b) U_T. (c) Violin plot of cumulative κ values.

H.2 Evaluation of Final model performance

After completion of all AL loops, the ensemble hierarchical ANN model was retrained using the full augmented dataset. Model accuracy was evaluated using both an independent held-out test set and a prospective fabrication test. Performance was quantified using the mean relative error (MRE):

$$\text{MRE} = \frac{1}{N}\sum_{i=1}^{N}\left|\frac{y_i - \hat{y}_i}{y_i}\right|, \tag{18}$$

where y_i and $\hat{y}_i$ denote the predicted and experimentally measured property values, respectively. The final ensemble achieved an average MRE of 17% among $\{\sigma_u, U_T, \kappa\}$ on the independent test set, while the prospective fabrication test yielded comparable accuracy, consistent with experimentally observed measurement variability ($\sim$15%). These results indicate that the combined use of shared-encoder architectures, uncertainty-informed data augmentation, and ensemble modeling yields robust predictive performance in small, heterogeneous experimental datasets.

Additionally, SHAP analysis results quantify the contributions of individual component loadings to each target property and are consistent with observed data distribution trends. Specifically, MMT exhibits the strongest positive contribution to σ_u, while CMC, CNC, CHS, and GLY contribute positively to tensile toughness U_T. For dielectric constant κ, GLY and metal oxide additives show dominant positive contributions, reflecting their role in enhancing polarization pathways. Together, these results demonstrate that the trained models capture physically meaningful and interpretable relationships that align with experimental observations.

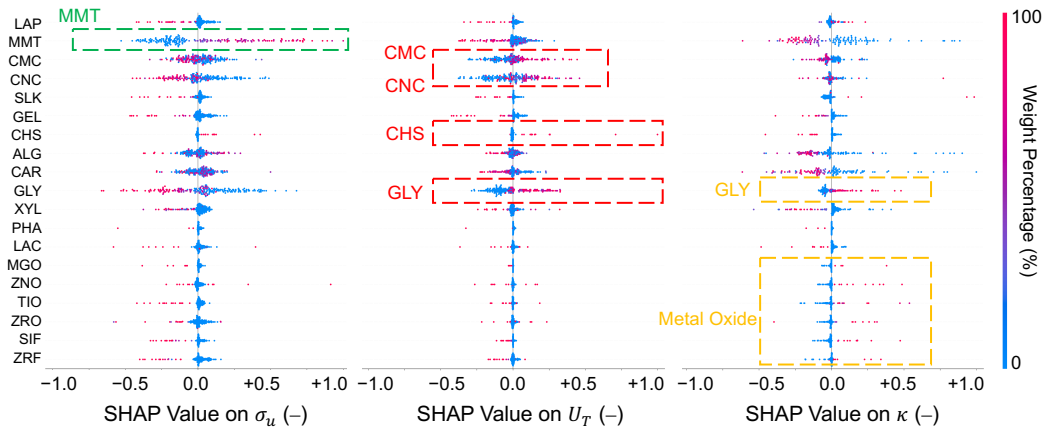

Figure 14: SHAP analysis results of σ_u, U_T, and κ after eight rounds of dynamic AL.

H.3 Benchmarking Against Baseline and Model-Driven Sampling Strategies

To rigorously evaluate sampling efficiency, the proposed multi-stage dynamic AL strategy was benchmarked against three representative baselines: random sampling, diversity sampling, and Bayesian optimization (BO). Random sampling serves as the primary (naive) baseline. At each iteration t, the next formulation C_{t+1} is selected uniformly at random from the remaining candidate pool,

$$C_{t+1} \sim U(\mathcal{X} \setminus D_t), \tag{19}$$

where $\mathcal{X}$ denotes the full feasible formulation space, C represents a formulation encoded as a composition vector, and $D_t = \{C_1, \ldots, C_t\}$ is the set of previously sampled formulations.

Diversity sampling represents a geometry-driven exploration heuristic that prioritizes coverage of the design space. At each step, the next formulation is selected to maximize its minimum Euclidean distance from previously sampled points,

$$C_{t+1} = \underset{C \in \mathcal{X}}{\operatorname{argmax}} \min_{C_i \in D_t} \|C - C_i\|_2, \tag{20}$$

Table 2: Performance comparison of dynamic active learning (AL) and baseline sampling strategies for σ_u and U_T optimization.

Sampling Strategy	$\boldsymbol{\sigma_u}$ (MPa)	$\boldsymbol{U_T}$ (MJ m^{-3})
Random Sampling	133.3	12.81
Diversity Sampling	126.2	14.05
Bayesian Optimization	153.0	17.15
Dynamic Active Learning	193.3	23.74

where $\|\cdot\|_2$ measures compositional dissimilarity between formulations.

BO is included as a surrogate-based baseline commonly used in materials discovery. A Gaussian Process (GP) model is trained on observed data to approximate the objective function $f(C)$, and new candidates are selected by maximizing an acquisition function. In this work, BO employs the Expected Improvement (EI) criterion,

$$EI(C) = E[\max(0, f(C) - f^* - \xi)], \tag{21}$$

where f^* is the best observed objective value, ξ is an exploration parameter controlling the exploration–exploitation tradeoff, and the expectation is taken with respect to the GP posterior.

Random sampling was selected as the primary baseline because it introduces no inductive bias or surrogate assumptions, providing a lower bound on achievable performance under uniform exploration. In high-dimensional, failure-prone formulation spaces with sparse and heterogeneous experimental feedback, random sampling serves as an unbiased reference for determining whether learning-guided acquisition yields performance gains beyond chance-level exploration. Diversity sampling and BO strategies were included as stronger baselines that incorporate additional structure. Diversity sampling explicitly promotes geometric coverage of the design space by favoring compositionally distant formulations, enabling exploration of under-sampled regions but without leveraging predictive performance or uncertainty. BO represents a surrogate-based optimization approach that balances exploration and exploitation through a learned model and acquisition function. While BO can achieve moderate improvements, its effectiveness degrades in high-dimensional formulation spaces with limited initial data and batch-executed experiments, consistent with prior observations in materials discovery settings.

All sampling strategies were evaluated under an identical experimental budget of 300 formulations. Each method was initialized with 10 randomly selected formulations, followed by a fixed allocation of 70 formulations in Stage 1, 170 formulations in Stage 2, and 50 formulations in Stage 3, matching the protocol used by the proposed dynamic AL framework. Performance was assessed using a high-accuracy oracle predictor to estimate achievable ultimate tensile strength (σ_u) and tensile toughness (U_T) across the candidate space. Each experiment was repeated over 128 independent runs with different random initializations to capture statistical variability (Figure 3).

Under identical budgets, random sampling and diversity sampling, both governed by stationary acquisition objectives, exhibited early saturation, plateauing at approximately 130 MPa in σ_u and 12–14 MJ m^{-3} in U_T. BO achieved moderate improvements, reaching $\sim$150 MPa in σ_u and $\sim$17 MJ m^{-3} in U_T, but showed diminished returns in the high-dimensional formulation space with limited initial data, consistent with known limitations of BO under batch execution and non-stationary objectives. In contrast, the proposed dynamic AL strategy consistently achieved the highest predicted performance, reaching $\sim$193 MPa in σ_u and $\sim$24 MJ m^{-3} in U_T within the same budget.

From a learning-theoretic perspective, these results (summarized in Table 2) highlight the advantage of stage-wise, non-stationary acquisition, which can be viewed as a form of curriculum learning over the design space. By explicitly transitioning from diversity-driven exploration to balanced exploration–exploitation and finally to objective-focused refinement, the proposed strategy adapts the acquisition objective to the evolving fidelity of the surrogate model and the structure of experimental feedback. This adaptive behavior provides a clear advantage over static acquisition rules, including BO, and enables more efficient navigation of complex, high-dimensional materials design problems.

I PREDICTIVE AND INVERSE DESIGN OF BIODEGRADABLE ELECTRONIC SUBSTRATES

We developed a predictive and inverse design framework that leverages the trained ensemble models to directly identify biobased nanocomposite formulations with targeted mechanical performance and tunable dielectric properties, avoiding exhaustive trial-and-error experimentation. Given a formulation C, the ensemble predicts σ_u, U_T, and κ, along with predictive uncertainty estimated from ensemble variance. To demonstrate this capability, the framework was applied to the design of flexible electronic substrates, which require mechanical robustness, defined as high toughness and moderate strength, and application-dependent dielectric behavior (low κ for inductive components and high κ for capacitive components).

Approximately three million feasible formulations were virtually sampled using a combination of random and diversity-based strategies. For each formulation, ensemble predictions and uncertainty were computed. Prediction uncertainty was quantified as:

$$\mathrm{Var}(C) = \frac{1}{N}\sum_{i=1}^{N}\left|\frac{y_i-\mu}{\mu}\right|^2 \times 100\%, \tag{22}$$

where N is the number of ensemble members, y_i is the prediction from the i-th model, and μ is the ensemble mean. Candidates exceeding a predefined uncertainty threshold were filtered out. Predicted property combinations were visualized in Figure 15 (σ_u–κ and U_T–κ) to identify regions satisfying multi-property constraints. Two representative design targets were considered: (i) mechanically robust substrates with low dielectric constant ($\sigma_u > 30$ MPa, $U_T > 15$ MJ m^{-3}, $\kappa < 3$) and (ii) mechanically robust substrates with high dielectric constant ($\sigma_u > 30$ MPa, $U_T > 15$ MJ m^{-3}, $\kappa > 40$). Cluster analysis of filtered candidates revealed compositionally coherent formulation families for each regime. The inverse design results highlighted distinct formulation–property trends, including CHS-based formulations plasticized with GLY/XYL for low-κ substrates and CMC/CNC-based matrices combined with metal oxides for high-κ substrates. These results demonstrate that the framework not only recommends viable formulations but also provides interpretable insights that support rational design of biodegradable electronic substrates across diverse functional requirements.

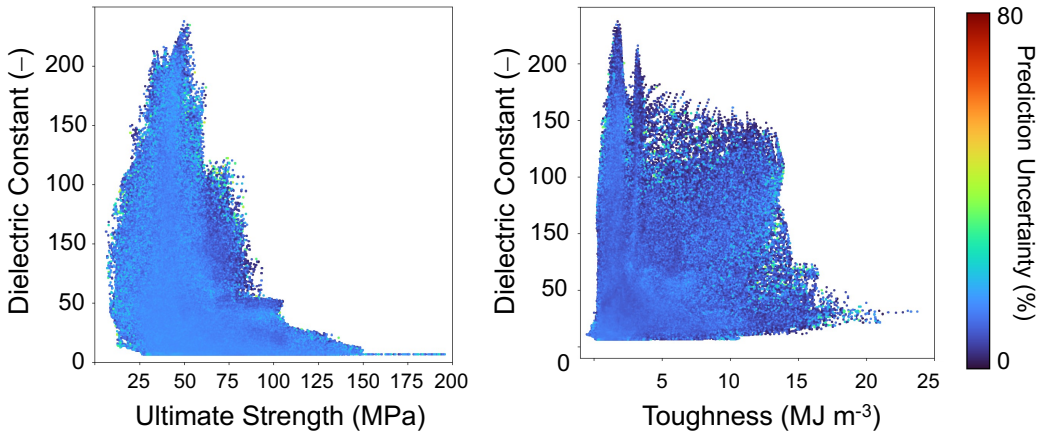

Figure 15: 2D heatmaps of ensemble predictions for σ_u–κ and U_T–κ, with color indicating normalized predictive uncertainty.